

Large Transverse and Longitudinal Magneto-Thermoelectric Effect in Polycrystalline Nodal-Line Semimetal Mg_3Bi_2

Tao Feng, Panshuo Wang, Zhijia Han, Liang Zhou, Wenqing Zhang,* Qihang Liu,* and Weishu Liu*

Topological semimetals provide new opportunities for exploring novel thermoelectric phenomena, owing to their exotic and nontrivial electronic structure topology around the Fermi surface. Herein, the discovery of large transverse and longitudinal magneto-thermoelectric (MTE) effects in Mg_3Bi_2 is reported and predicted to be a type-II nodal-line semimetal in the absence of spin-orbit coupling (SOC). The maximum transverse power factor is $2182 \mu\text{W m}^{-1}\text{K}^{-2}$ at 13.5 K and 6 Tesla. The longitudinal power factor reaches up to $3043 \mu\text{W m}^{-1}\text{K}^{-2}$, which is 20 times higher than that in a zero-strength magnetic field and is also comparable to state-of-the-art MTE materials. By compensating the Mg loss in Mg-rich conditions for tuning the carrier concentration close to intrinsic state, the sample fabricated in this study exhibits a large linear non-saturating magnetoresistance of 940% under a field of 14 Tesla. Using density functional calculations, the authors attribute the underlying mechanism to the parent linear-dispersed nodal-line electronic structure without SOC and the anisotropic Fermi surface shape with SOC, highlighting the essential role of high carrier mobility and open electron orbits in the moment space. This work offers a new avenue toward highly efficient MTE materials through defect engineering in polycrystalline topological semimetals.

1. Introduction

Magneto-thermoelectric (MTE) effects include both transverse and longitudinal transport properties, depending on the directions of the magnetic field (B), temperature gradient ($\partial T/\partial r$), and voltage drop ($\partial V/\partial r$). Transverse-MTE is known as the Nernst effect,^[1,2] wherein a nonzero $\partial V/\partial r$ occurs along the y -axis if the $\partial T/\partial r$ is along the x -axis and B along the z -axis.


Longitudinal-MTE constitutes the magneto-Seebeck effect,^[3,4] where nonzero $\partial V/\partial r$ occurs along the x -axis if $\partial T/\partial r$ is along the x -axis and B along the z -axis. The magnetic field plays a role of tuning the carrier transport, broadening the scope of the conventional thermoelectric effect for waste-heat harvesting and solid-state cooling.^[5–7] Over the past years, significant progress has been made in the field of conventional thermoelectric materials through nanoscale engineering techniques, such as introducing various atomic defects, nano-inclusions, and grain boundaries.^[8–10] By contrast, the MTE effect is susceptible to defects. Consequently, most previous studies have focused on the MTE effect in single crystals.^[11,12] For instance, by applying a magnetic field, Chen et al. observed performance enhancement in the transverse power factor manipulated by the bipolar effect, which is the main Seebeck coefficient restriction in the power factor, and a transverse power factor of $400 \mu\text{W cm}^{-1}\text{K}^{-2}$ was achieved at 30 K and 10 Tesla in single-crystal

semimetal Mg_2Pb .^[13] Compared with single-crystal materials, polycrystalline samples have obvious advantages in easily synthesizing large size samples, but challenges to tune the Fermi level towards the intrinsic state. As a result, the polycrystalline MTE materials have not yet gotten wide attention.

Fundamentally, MTE materials typically require an ultrahigh carrier mobility, electron–hole compensation, and a small Fermi surface.^[2,14,15] Hence, topological semimetals are promising MTE materials because of their linear-dispersed low-energy excitation and special topological surface states.^[4,16] Weyl semimetals and Dirac semimetals usually exhibit very high mobility owing to their massless Weyl and Dirac quasiparticles.^[17–19] In addition, particle-hole-like symmetry usually exists in both Weyl and Dirac semimetals, in which the linear bands have led to almost equal concentrations of electron and hole carriers. In addition, the Fermi surface is tiny when the chemical potential is located around the charge-neutral band-crossing point. This could result in non-saturating magnetoresistance (MR) according to the electron–hole compensation mechanism based on the double carrier model,^[20] as well as potentially a large longitudinal thermopower (see Part I, Supporting Information). Recently, large MTE effects were predicted theoretically in Weyl/Dirac semimetals,^[3] and high thermoelectric performances

T. Feng, Z. Han, W. Zhang, W. Liu
Department of Materials Science and Engineering
Southern University of Science and Technology
Shenzhen 518055, China
E-mail: zhangwq@sustech.edu.cn; liuws@sustech.edu.cn

P. Wang, L. Zhou, Q. Liu
Department of Physics and Shenzhen Institute for Quantum Science & Engineering
Southern University of Science and Technology
Shenzhen 518055, China
E-mail: liuqh@sustech.edu.cn

 The ORCID identification number(s) for the author(s) of this article can be found under <https://doi.org/10.1002/adma.202200931>.

DOI: 10.1002/adma.202200931

were observed in experiments.^[21–25] Polycrystalline Weyl semimetal NbP shows a transverse thermopower of $90 \mu\text{V K}^{-1}$ and a maximum transverse power factor of $3500 \mu\text{W m}^{-1}\text{K}^{-2}$ at 136 K and 9 T, while its longitudinal power factor is only $850 \mu\text{W m}^{-1}\text{K}^{-2}$ at 100 K and 9 Tesla.^[22] Wang et al. reported that the power factor of Dirac semimetal Cd_3As_2 single-crystal greatly increased under a perpendicular magnetic field, yielding power factor increase from 2150 to $4700 \mu\text{W m}^{-1}\text{K}^{-2} \approx 350 \text{ K}$.^[23] Liang et al. found a transverse power factor of $2100 \mu\text{W m}^{-1}\text{K}^{-2}$ at 300 K and 10 Tesla in single-crystal $\text{Pb}_{0.77}\text{Sn}_{0.23}\text{Se}$, and raised that gap inversion can change the sign of the Nernst signal.^[24] Fu et al. reported the MTE effect in single-crystal Dirac semimetal PtSn_4 , which shows a transverse thermopower reaches a moderate value of $45 \mu\text{V K}^{-1}$ at 10.3 K and 9 Tesla and longitudinal thermopower of $40 \mu\text{V K}^{-1}$ at 15 K and 9 Tesla.^[25] In addition, MTE properties are also studied in other topological semimetals such as TaAs family (i.e., TaAs, TaP, and NbAs),^[26] Fe_3Sn_2 ,^[27] CoSi ,^[28] W_2As_3 ,^[29] PrAlGe ,^[30] etc.

As a novel type of topological semimetal, Mg_3Bi_2 -based materials exhibit excellent thermoelectric properties at room temperature.^[31] Recent first-principles calculations have shown that a type-II nodal line appears in the k_x - k_y plane of the Brillouin zone, while a pair of Dirac points exists along the k_z axis^[32] when spin-orbit coupling (SOC) is considered. However, the Mg_3Bi_2 single-crystal bulk provided a MR of only 3% at 2 K and 9 Tesla, indicating that its magnetic response was much weaker than that of other topological semimetals.^[33] Zhou et al. measured the longitudinal-MTE properties of Mg_3Bi_2 films, which also exhibited a weak MR of 0.6% at 2 K and 2 Tesla.^[34] Notably, Mg_3X_2 ($\text{X} = \text{Bi}, \text{Sb}$) samples usually have a high concentration of Mg vacancies because of the low formation energy. Therefore, the previously observed weak MR or MTE responses might not be from the intrinsic behavior of type-II nodal line semimetal, but due to the scattering of Mg vacancies.

Herein, we report the discovery of significantly boosted transverse and longitudinal MTE effects in Mg_3Bi_2 polycrystalline bulk samples that were synthesized under Mg-rich conditions. Through the systematic composition control, we obtain the sample closest to the intrinsic state of the Mg_3Bi_2 nodal-line semimetal. It exhibits a large transverse thermopower and longitudinal thermopower of up to $127 \mu\text{V K}^{-1}$ at 13.5 K and $176 \mu\text{V K}^{-1}$ at 15 K, respectively. In response, the maximum transverse and longitudinal power factors reach 2182 and $3043 \mu\text{W m}^{-1}\text{K}^{-2}$, respectively, for the as-fabricated Mg_3Bi_2 polycrystalline sample. The measured electron and hole mobilities are 4843 and $1393 \text{ cm}^2 \text{ V}^{-1}\text{s}^{-1}$, respectively, an order of magnitude higher than the previously reported values for Mg_3Bi_2 .^[33,34] In addition, polycrystalline Mg_3Bi_2 clearly shows a linear unsaturated MR of up to 940% at 2 K and 14 Tesla. Our theoretical calculations based on density functional theory (DFT) reveal a strongly anisotropic MR in Mg_3Bi_2 due to the anisotropic Fermi surface shape, resulting in large transverse and longitudinal MTE effects. These findings highlight the great potential of Mg_3Bi_2 -based materials for energy conversion through the MTE effect, providing a new route for exploring high-performance polycrystalline MTE materials in the family of nodal-line semimetals through the defect engineering.

2. Results

2.1. Defects Engineering toward the Intrinsic Nodal-Line Semimetal Mg_3Bi_2

Mg_3Bi_2 has a crystalline structure with a trigonal lattice and space group $\text{P}\bar{3}\text{m}1$ (Figure S1a, Supporting Information).^[35] Bi is located in the interior of a single cell, while Mg usually has two positions: vertex Mg (Mg-1: 0, 0, 0) and interior Mg (Mg-2: 0.3333, 0.6667, 0.6300). The Mg at the vertex site can be easily lost during synthesis process, leading to the formation of Mg vacancy defects.^[36] Consequently, polycrystalline bulk Mg_3Bi_2 synthesized by high-temperature processes usually tends to present p-types, similar to the situation in Mg_3Sb_2 .^[37] In addition, Mg vacancy could also scatter the carriers, resulting in limited mobility as reported previously for Mg_3Bi_2 single-crystal bulks.^[33]

To suppress Mg vacancies and optimize carrier mobility, a series of Mg_3Bi_2 samples with a nominal composition of $\text{Mg}_{3+x}\text{Bi}_2$ ($x = 0, 0.1, 0.2, 0.3, 0.4, \text{ and } 0.5$) were successfully synthesized under different Mg compensations with nominal composition using mechanical alloying and spark plasma sintering (SPS) (Table S1, Supporting Information). Among the as-fabricated polycrystalline Mg_3Bi_2 samples [indexed as sample #1 ($x = 0$), #2 ($x = 0.1$), #3 ($x = 0.2$), #4 ($x = 0.3$), #5 ($x = 0.4$), and #6 ($x = 0.5$) with different Mg-rich nominal compositions], sample #5, that is, $\text{Mg}_{3.4}\text{Bi}_2$, is determined to be closest to the intrinsic state of the Mg_3Bi_2 nodal-line semimetal through Hall resistivity and thermal conductivity measurements (refer to Part II and Figures S1–S4, Supporting Information). The intrinsic state is a critical requirement for optimizing the carrier mobility and intrinsic Fermi surface shape to enhance the MTE effect.^[38] Through the double carrier model for Hall resistivity ρ_{xy} .^[39]

$$\rho_{xy} = \frac{1}{e} \frac{(n_h \mu_h^2 - n_e \mu_e^2) + \mu_h^2 \mu_e^2 B^2 (n_h - n_e)}{(n_h \mu_h + n_e \mu_e)^2 + \mu_h^2 \mu_e^2 B^2 (n_h - n_e)^2} B \quad (1)$$

The carrier mobility of the obtained Mg_3Bi_2 sample in this work is calculated as $\mu_e = 4843 \text{ cm}^2 \text{ V}^{-1}\text{s}^{-1}$ and $\mu_h = 1393 \text{ cm}^2 \text{ V}^{-1}\text{s}^{-1}$, which is much higher than reported single-crystal bulk ($450 \text{ cm}^2 \text{ V}^{-1}\text{s}^{-1}$) and single-crystal film Mg_3Bi_2 materials ($120 \text{ cm}^2 \text{ V}^{-1}\text{s}^{-1}$) in previous studies.^[33,34]

2.2. Large Transverse and Longitudinal Magneto-Thermoelectric (MTE) Effect

Figure 1 shows the transverse-MTE and longitudinal-MTE properties of the as-fabricated polycrystalline Mg_3Bi_2 (sample #5) with a nominal composition of $\text{Mg}_{3.4}\text{Bi}_2$. To study the transverse-MTE properties, that is, Nernst effect of the Mg_3Bi_2 sample, we measured the transverse thermopower S_{xy} (i.e., $\partial I/\partial r$ along x -axis, $\partial V/\partial r$ along y -axis, and B along z -axis) at 1, 3, 6, 9, and 13 Tesla at temperatures range from 2 to 275 K. S_{xy} increases with the increasing magnetic field and reaches a peak value of $127 \mu\text{V K}^{-1}$ at 13 Tesla and 13.5 K (Figure 1a), which exceeds the previously reported values for polycrystalline NbP,^[22] and is comparable to that of single-crystal $\text{Pb}_{0.77}\text{Sn}_{0.23}\text{Se}$

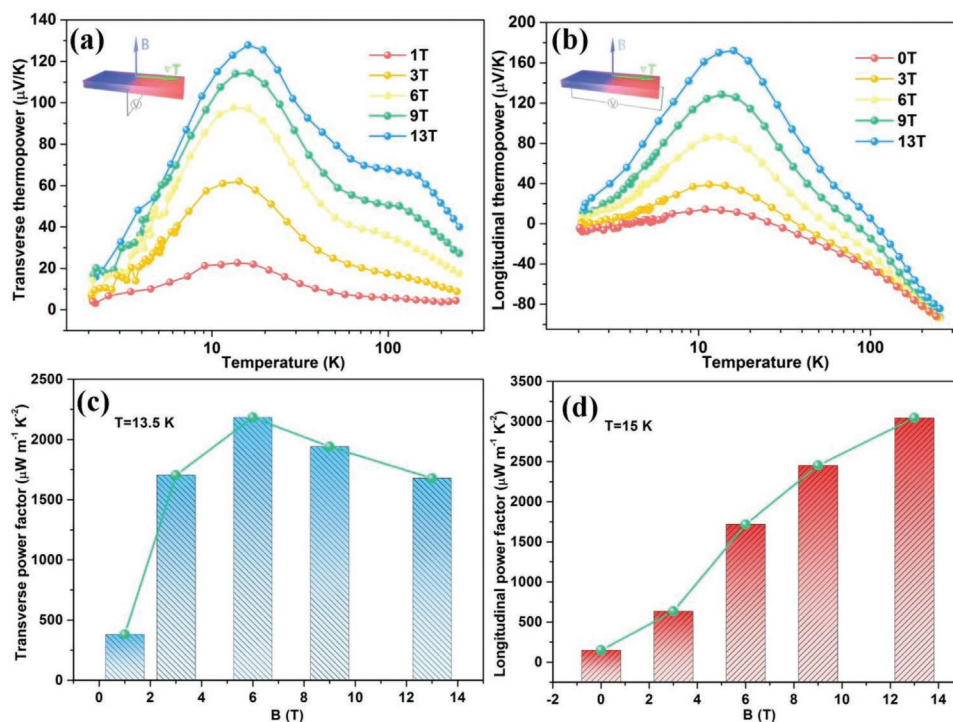


Figure 1. Transverse- and longitudinal-MTE properties of polycrystalline Mg_3Bi_2 . a) The transverse thermopower and b) longitudinal thermopower of Mg_3Bi_2 under different magnetic fields in a temperature range of 2 and 275 K. c) Changes in transverse power factor and d) longitudinal power factor of Mg_3Bi_2 with increasing magnetic field at 13.5 and 15 K, respectively.

in the low magnetic field range.^[24] A more detailed comparison is presented in Figure S5, Supporting Information. The higher transverse thermopower, the higher Nernst coefficient, in accordance with $N_{xy} = S_{xy}/\mu_0 H$ (Figure S6, Supporting Information).^[40] The Nernst coefficient of the as-fabricated polycrystalline Mg_3Bi_2 gradually decreases with the increase of magnetic field, consistent with the behavior of other topological materials.^[41]

The temperature-dependent longitudinal thermopower was measured under different magnetic fields to examine the longitudinal-MTE properties (magneto-Seebeck effect). Figure 1b shows the longitudinal thermopower of the Mg_3Bi_2 sample at 0, 3, 6, 9, and 13 Tesla in a temperature range of 2 and 275 K, reaching a maximum value of $176 \mu\text{V K}^{-1}$ at 15 K and 13 Tesla, which corresponds to 13 times enhancement. The longitudinal-MTE effect of Mg_3Bi_2 is also sensitive to the Mg-rich conditions (Figure S7a, Supporting Information), which is consistent with the carrier mobility and MR. Compared to other MTE materials, the as-fabricated Mg_3Bi_2 shows superior gains in longitudinal thermopower under the magnetic field (Figure S7b, Supporting Information). Of note, the longitudinal thermopower in the as-fabricated Mg_3Bi_2 remained unsaturated up to a magnetic field of 14 Tesla (Figure S8, Supporting Information). The observed high and non-saturating longitudinal thermopower in the as-fabricated Mg_3Bi_2 should be relative to the special Fermi surface of nodal-line semimetals. Recently, Skinner and Fu theoretically predicted a large and non-saturating thermopower in Dirac/Weyl semimetals subjected to a quantized magnetic field,^[3] which was supported by the experimental work on Dirac semimetals $\text{Pb}_{1-x}\text{Sn}_x\text{Se}$ and Cd_3As_2 .^[23,24] The longitudinal

thermopower feature found in Mg_3Bi_2 illustrates that the large and non-saturating thermopower could also be extended to nodal-line semimetals. The transverse power factor P_{xy} and longitudinal power factor P_{xx} can be calculated by:^[22]

$$P_{xx} = S_{xx}^2 \sigma_{xx} \quad (2a)$$

$$P_{xy} = S_{xy}^2 \sigma_{yy} \quad (2b)$$

The as-fabricated Mg_3Bi_2 is a polycrystalline material, and consequently, the electrical conductivity is isotropic; thus, σ_{xx} should be equal to σ_{yy} . The calculated P_{xy} and P_{xx} values for different magnetic fields are plotted in Figures 1c and 1d, respectively. As the magnetic field strength increased, the transverse power factor P_{xy} of Mg_3Bi_2 shows a peak at 6 Tesla, while the longitudinal power factor P_{xx} exhibits unsaturated growth. The highest unsaturated P_{xx} is $3043 \mu\text{W m}^{-1}\text{K}^{-2}$ at 15 K under 13 Tesla, which is 20 times higher than the value at zero magnetic field strength. This value is also higher than that of most previously reported MTE materials, such as polycrystalline NbP ($850 \mu\text{W m}^{-1}\text{K}^{-2}$ at 100 K and 9 Tesla), polycrystalline Ag_2Se ($\approx 1250 \mu\text{W m}^{-1}\text{K}^{-2}$ at 300 K and 5 Tesla), single-crystal FeGe_2 ($625 \mu\text{W m}^{-1}\text{K}^{-2}$ at 250 K and 9 Tesla), and single-crystal Cd_2As_3 ($2500 \mu\text{W m}^{-1}\text{K}^{-2}$ at 450 K and 7 Tesla).^[22,42–44] Besides, the highest P_{xy} of $2182 \mu\text{W m}^{-1}\text{K}^{-2}$ at 13.5 K and 6 Tesla, obtained in the as-fabricated polycrystalline Mg_3Bi_2 , is higher than polycrystalline Ag_2Se ($\approx 35 \mu\text{W m}^{-1}\text{K}^{-2}$ at 300 K and 5 Tesla), polycrystalline $\text{Bi}_{77}\text{Sb}_{23}$ ($540 \mu\text{W m}^{-1}\text{K}^{-2}$ at 50 K and 5 Tesla), and comparable to single-crystal $\text{Pb}_{0.77}\text{Sn}_{0.23}\text{Se}$ ($2100 \mu\text{W m}^{-1}\text{K}^{-2}$ at 300 K and 10 Tesla), single-crystal Re_4Si_7 ($\approx 2100 \mu\text{W m}^{-1}\text{K}^{-2}$ at

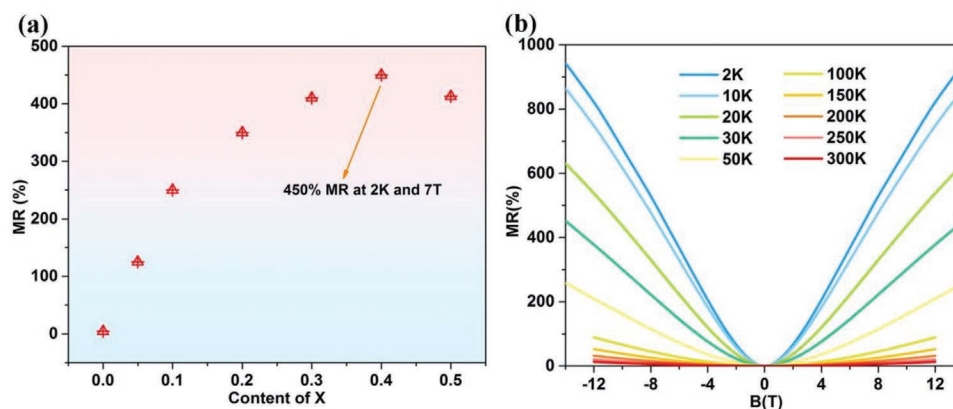


Figure 2. MR properties of polycrystalline Mg₃Bi₂. a) The MR of the as-fabricated polycrystalline Mg_{3+x}Bi₂ ($x = 0, 0.1, 0.2, 0.3, 0.4, 0.5$) at 2 K and 7 Tesla (Table S1, Supporting Information). b) The MR of sample #5 with a nominal composition of Mg_{3.4}Bi₂ at different temperatures in a magnetic field of up to 14 Tesla.

550 K and 1.4 Tesla), and close to the value for polycrystalline NdP ($3500 \mu\text{W m}^{-1}\text{K}^{-2}$ at 150 K and 9 Tesla).^[22,24,44–46] Furthermore, at low-temperature near 15 K, the MTE power factors of P_{xx} and P_{xy} are much higher than those of conventional thermoelectric materials (Figure S9, Supporting Information), demonstrating the advantages of MTE materials.

2.3. Large Magnetoresistance (MR) Effect

The key features of MTE materials with large transverse thermopower have been typically attributed to ultrahigh carrier mobility and electron–hole compensation, which are the exact conditions required for large MR. Owing to the presence of electrons and holes, topological semimetals usually exhibit very high MR, which is even not saturating at higher magnetic field strengths of tens of Tesla.^[47,48] Its electrical conductivity σ can be significantly modulated under a magnetic field (Part III, Supporting Information), modifying MR and improving the longitudinal thermopower (Part I, Supporting Information). Therefore, the MR, which reflects the response of the electrical transport properties to a magnetic field, is closely related to the MTE effect. **Figure 2a** compares the MR of the as-fabricated polycrystalline Mg₃Bi₂ specimens with different nominal compositions of Mg_{3+x}Bi₂ ($x = 0, 0.1, 0.2, 0.3, 0.4$, and 0.5) at 2 K and 7 Tesla. Detailed MR measurements are shown in Figure S10, Supporting Information. All the samples fabricated in this study have positive MR values between 2 and 300 K. Of note, the MR of sample #1 with a nominal composition of Mg₃Bi₂ is very close to previously reported Mg₃Bi₂ materials in the literature.^[33,49] It suggested the coupling between electric transport and the magnetic field is highly sensitive to the Mg vacancies in Mg₃Bi₂. The MR of Mg₃Bi₂ at 2 K and 7 Tesla increases from 4% to 250%, 350%, 410%, 450%, and 413% as the nominal Mg-rich content x increased from $x = 0$ to 0.1, 0.2, 0.3, 0.4, and 0.5, respectively. Sample #5, with a nominal composition of Mg_{3.4}Bi₂, shows a recording value of 940% at 2 K and 14 Tesla, which is two orders of magnitude higher than that of previously reported Mg₃Bi₂ single crystals.^[33,34] Notably, the MR is still unsaturated even at a magnetic field strength of up to 14 Tesla. Additionally, excessive Mg decreases

the MR (sample #6, nominal composition of Mg_{3.5}Bi₂), further suggesting that sample #5 is closest to the intrinsic state of a semimetal.

2.4. Anisotropic MR

To understand the anomalous behavior of MR, we performed DFT electronic structure calculations as well as DFT-based transport calculations to simulate the variance of MR as a function of the external magnetic field along the x and z directions. Without considering SOC, the band crossing was close to the Fermi level, showing the type-II nature of the nodal line in Mg₃Bi₂ (Figure S11, Supporting Information). When including SOC, a small energy gap (≈ 40 meV, as shown in **Figure 3a**) at the nodal points is opened. The corresponding electrical conductivity tensor σ of Mg₃Bi₂ was obtained by applying the following formula:^[50,51]

$$\sigma = \sum_n \sigma^{(n)} = \sum_n \frac{e^2}{4\pi^3} \int dk \tau [\varepsilon_n(k)] v_n(k) \bar{v}_n(k) \left(-\frac{\partial f}{\partial \varepsilon} \right)_{\varepsilon=\varepsilon_n(k)} \quad (3)$$

where e is the electron charge, $\varepsilon_n(k)$ is the n th band energy at the momentum k in the Brillouin zone with the corresponding relaxation time $\tau[\varepsilon_n(k)]$, $\bar{v}_n(k)$ is the weighted average of the Fermi velocity $v_n(k)$, and f is the Fermi distribution function of the equilibrium state. The total conductivity σ is a summation of the individual band contribution $\sigma^{(n)}$; the MR, that is, the resistivity tensor ρ , can be obtained by inverting the conductivity tensor σ (i.e., $\rho = \sigma^{-1}$). Equation (3) was calculated based on the tight-binding model by Wannier representation extracted from DFT wavefunctions^[52,53] (Part III, Supporting Information). In addition, a constant relaxation-time approximation was adopted.^[52–54] The weighted average group velocity $\bar{v}_n(k)$ reflects the nonlinear influence of the magnetic field on the electrical conductivity. A larger magnetic field involves more k points' average (Equation (S8)), leading to saturating or non-saturating MR behavior.

The calculated transport results are shown in Figures 3c–f. The Fermi level was set to $E_f = 0.19$ eV (i.e., blue line in Figure 3a), corresponding to the as-fabricated sample

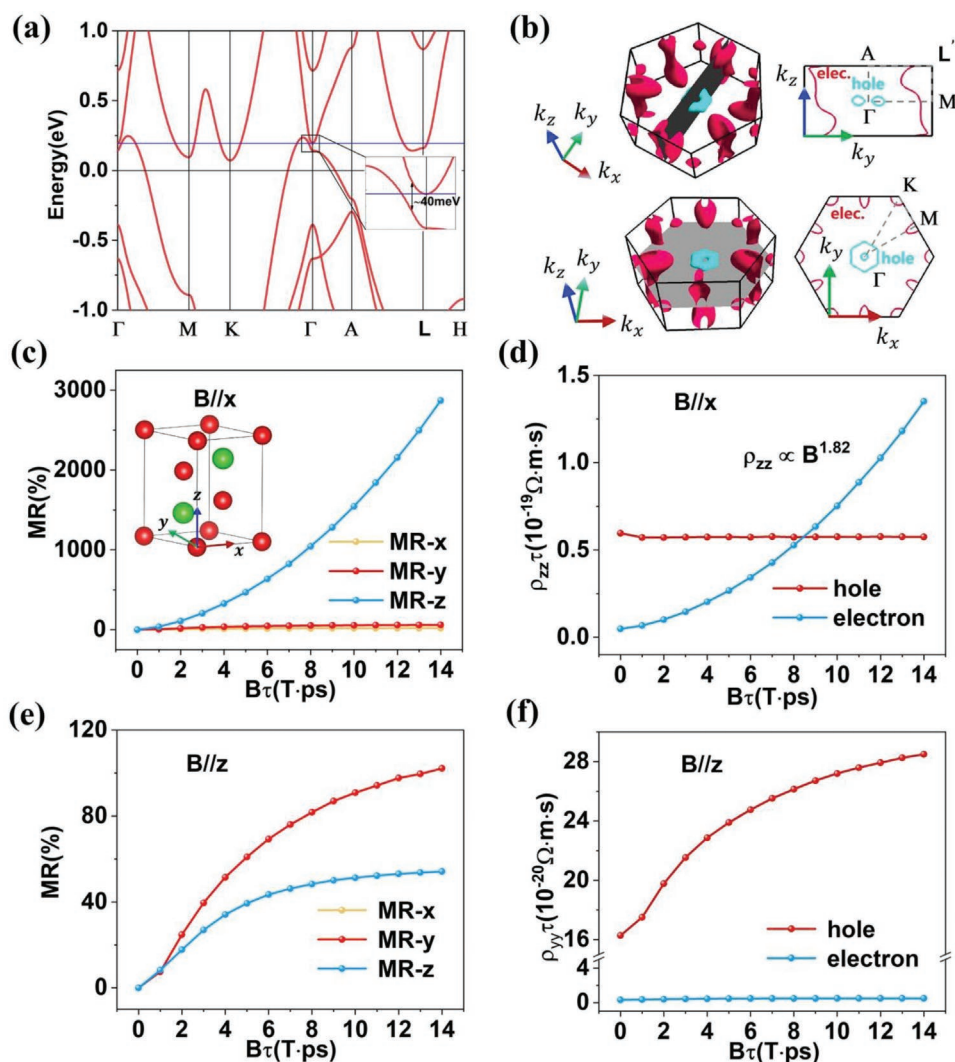


Figure 3. Electronic structure and transport properties of Mg_3Bi_2 from first-principles calculations. a) Band structure of Mg_3Bi_2 with SOC, where the blue line is the approximated Fermi level for Mg_3Bi_2 within the rigid band model. b) Fermi surface of Mg_3Bi_2 (left panel). The cross-section of the Fermi surface was produced by the $k_x = 0$ (upper right) and $k_z = 0$ (bottom right) planes, respectively, exhibiting “open” orbits of electrons along k_z and “closed” orbits of holes within the $k_y - -k_z$ plane (i.e., $B//x$), and the “closed” orbits of both electrons and holes in the $k_x - -k_y$ plane (i.e., $B//z$). c–f) Field dependence of MR along the x (yellow), y (red), and z (blue) directions with c) $B//x$ and e) $B//z$, respectively. The inset in (c) shows the crystal structure. Field dependence of separate contributions of electrons (blue) and holes (red) on the electrical resistivities d) ρ_{zz} for $B//x$ and f) ρ_{yy} for $B//z$.

#5 Mg_3Bi_2 obtained in this work, where the carrier mobility is optimal because of the change in the carrier effective mass (refer to Table S2 in Part IV, Supporting Information). This is also the band crossing point of the nodal line. First, an anisotropic MR was observed in hexagonal Mg_3Bi_2 when the magnetic field was applied along the x axis (Figure 3c). The z -axis MR showed a nearly quadratic increase with the magnetic field, whereas the y -axis MR and x -axis MR were significantly smaller and rapidly saturated with B (Figure 3c). We obtained a large and unsaturated z -axis MR of near 3000% at $B\tau = 14$ (Tesla \cdot ps) ($B//x$). On the other hand, when $B//z$ (Figure 3e), MR saturated in all three directions, approaching no more than 105%. Owing to the in-plane rotational symmetry under a perpendicular magnetic field, the MR along the x and y directions are degenerate.

2.5. Fermi Surface Topology

To explain the anisotropic MR behavior, we studied the Fermi surface topology of the Bloch electrons and the trajectories of the charge carriers driven by the Lorentz force. Figure 3b shows the Fermi-surface contours with $E_f = 0.19$ eV (blue line in Figure 3a). Based on the semiclassical scenario (refer to Equation (S9) in Part III, Supporting Information), the directions of the magnetic field B , Fermi velocity $v_n(k(t))$, and derivative of k (i.e., \dot{k}) are perpendicular to each other. Thus, the orbits of the Bloch electrons in the Brillouin zone are the cross-sections of the Fermi surface and a plane which is simultaneously normal to B crossing the $k(t = 0)$ point. For $B//x$, the Fermi surface of the $k_x = 0$ plane is shown in the upper-right panel of Figure 3b. The hole orbits near the Gamma (Γ) point are closed

circles, while the electron orbits are open, that is, extending throughout the Brillouin zone along the k_z direction, resulting in fewer electrons moving along the z direction compared to the zero magnetic field condition. As a result, with an increase in magnetic field strength along x , the average velocity of the electrons along z decreases significantly (refer to Equation (S8) in Part III, Supporting Information), resulting in an increased resistivity ρ_{zz} . To confirm this, we theoretically separated the contributions of the electrons and holes for resistivity ρ_{zz} , as shown in Figure 3d. Electron resistivity exponentially increased with $B\tau$ with a power factor of 1.82, while the hole contributions remained nearly unchanged upon magnetic field, consistent with the understandings of orbit topology.

For $B//z$, the orbits of both the electrons and holes are closed (bottom right, Figure 3b), leading to the saturation properties of MR for all the directions. The separate contributions of the electrons and holes for ρ_{yy} shown in Figure 3f further confirm the closed-orbit nature of the Fermi surface. Considering that our experimental sample is polycrystalline, the total MR calculated by an average of all directions in a first-order approximation is consistent with our experimental results.

The above results imply that we could choose the optimal doping level in experiment to obtain large MR as well as MTE by designing the Fermi surface topology. Specifically, the Fermi level at $E_f = 0.19$ eV of Mg_3Bi_2 is optimal for nonsaturated MR, where the high carrier mobility and open carrier orbits occur simultaneously. On the other hand, the nonsaturated MR effect will be suppressed as the Fermi level moves away from the optimal value, which is consistent with our MR measurements for various Mg doping levels (Figure 2a and Figure S12, Supporting Information). For example, when $E_f = 0.15$ eV, both the electron and hole orbits are almost closed (Figure S13a, Supporting Information), leading to a saturated MR for Mg_3Bi_2 (Figures S12a and S12b, Supporting Information); when the Fermi level is further increased to 0.21 eV, more electron orbits around Γ are closed, not favorable for nonsaturated MR as well (Figures S12c, S12d, and S13c, Supporting Information). Of note, MR is small and saturated for the parent electronic structure without SOC at the band crossing point (Figure S14, Supporting Information). This indicates that the nodal-line semimetal with a tiny energy gap is a promising candidate system for realizing large MTE.

3. Conclusion

In summary, the large transverse and longitudinal MTE effects in a polycrystalline nodal-line semimetal Mg_3Bi_2 were investigated herein. Extra Mg compensation effectively inhibited the formation of Mg vacancy defects, rendering the sample with a nominal composition of $\text{Mg}_{3.4}\text{Bi}_2$ was very close to the stoichiometric state. Remarkably, polycrystalline Mg_3Bi_2 (sample #5, with a nominal composition of $\text{Mg}_{3.4}\text{Bi}_2$) shows a high transverse thermopower of $127 \mu\text{V K}^{-1}$ and longitudinal thermopower of $176 \mu\text{V K}^{-1}$ at 13 Tesla. The transverse power factor is $2182 \mu\text{W m}^{-1}\text{K}^{-2}$ at 13.5 K, while the longitudinal power factor reaches up to $3043 \mu\text{W m}^{-1}\text{K}^{-2}$ at 15 K, 20 times higher than those measured without magnetic field. Meanwhile, the MR of Mg_3Bi_2 gradually increases and reached a maximum value

of 940% at 14 Tesla and 2 K, indicating the positive correlation between MR and MTE effects. First-principles calculations revealed that the unsaturated MR behavior originates from the anisotropic Fermi surface topology of Mg_3Bi_2 , owing to the hexagonal crystal structure and parent nodal-line electronic structure. With SOC, the nodal line opens a small gap, resulting in nonsaturating MR as well as a large thermopower. Therefore, our work provides a general strategy to boost the MTE properties of topological materials through composition control, which would initiate a wide interesting in exploring the new MTE materials from the nodal-line semimetals.

4. Experimental Section

Sample Preparation: The $\text{Mg}_{3+x}\text{Bi}_2$ samples were synthesized through a combined approach of mechanical alloying and SPS. Magnesium turnings (Mg, 99.98%, Acros Organics) and bismuth shots (Bi, 99.999%, 5N Plus) were weighed according to the composition of $\text{Mg}_{3+x}\text{Bi}_2$ ($0 \leq x \leq 0.5$), and were loaded into a stainless-steel ball milling jar in a glove box under an Ar atmosphere with an oxygen level of <1 ppm. After ball milling for 10 h in a SPEX 8000M mixer, the ball-milled powders were loaded into a graphite die with an inner diameter of 15 mm, in the glove box. The graphite die with the loading powder was immediately sintered at 700°C under a pressure of 50 MPa for 5 min via SPS (SPS-211Lx, Fuji Electronic Industrial Co. LTD). The SPS bulks were ≈ 15 mm in diameter, with a thickness of ≈ 8 mm.

Sample Characterization: The phase purity of the product was measured by powder X-ray diffraction (XRD) on a Rigaku D/Max-2550 instrument (Cu $K\alpha$ radiation, $\lambda = 1.5418 \text{ \AA}$, 18 KW). The temperature-dependent thermal conductivity was measured adiabatically using the thermal transport option (TTO) on a Quantum Design Physical Property Measurement System (PPMS 14 Tesla) with one-heater and two-thermometer configuration. With the same option, the transverse and longitudinal thermopower were simultaneously measured adiabatically. The authors mounted the sample with transverse voltage leads, which were purposefully offset by a distance X from each other so that the longitudinal (Seebeck) and transverse (Nernst) voltage could both be measured. The heat flowed from left to right, and the thermometers T-hot and T-cold were mounted on the left and right leads located on the lower side of the sample. The V_+ and V_- leads measured the diagonal voltage component, and by measuring it as a function of the magnetic field in both the positive and negative fields, they could employ symmetry arguments to separate the longitudinal thermopower from the transverse thermopower. The longitudinal and Hall resistivities were measured using the electronic transport option (ETO) in Physical Property Measurement System (PPMS) using the standard four-probe method.

Calculation Methods: Electronic structure calculations were based on the DFT implemented in the Vienna ab initio simulation package (VASP),^[55,56] where the exchange-correlation potential was treated by generalized gradient approximation (GGA) of the Perdew–Burke–Ernzerhof (PBE) functional^[57] and the ionic potential was based on the projector augmented wave (PAW) method.^[58,59] Owing to the strong relativistic effect in Bismuth, SOC was also considered for the energy band dispersion calculations. The energy cutoff of the plane wave was set to 600 eV. For Brillouin zone sampling, a $19 \times 19 \times 9 \Gamma$ centered K-point mesh was used for the 5-atom unit cell for self-consistent calculations, and an $11 \times 11 \times 5$ mesh was used for structure relaxation. The convergence criteria of the energy and force were set to 10^{-6} eV and $0.002 \text{ eV \AA}^{-1}$, respectively. The tight-binding model Hamiltonian adapted for the Wannier interpolation implemented in the WannierTools package^[52,53] (i.e., electrical conductivity calculation) was constructed by the Wannier90 software^[60] using the maximally localized Wannier function approach.^[61–63] The s, p orbitals of Mg and p orbitals of Bi were selected as the initial projectors for Wannier90 software.

Statistical Analysis: The data in the work were obtained through necessary transformation and normalization. XRD patterns shown in Figure S1b, Supporting Information, were normalized to have identical maximum intensity. The Origin software was used to analyze and process data.

Supporting Information

Supporting Information is available from the Wiley Online Library or from the author.

Acknowledgements

T.F. and P.W. contributed equally to this work. This work was supported by the National Key R&D Program of China (2019YFA0704900), Shenzhen Science and Technology Basic Research Program (GXWD20201230110313001), Guangdong Innovative and Entrepreneurial Research Team Program (2016ZT06G587) and Shenzhen Science Technology Fund (KYDPT20181011104007). The authors would like to thank the support of Core Research Facilities (SCRF) of Southern University of Science and Technology. W.L. acknowledges the support from the Tencent Foundation through the XPLOER PRIZE.

Conflict of Interest

The authors declare no conflict of interest.

Data Availability Statement

The data that support the findings of this study are available from the corresponding author upon reasonable request.

Keywords

defect engineering, Fermi surface topology, magnetoresistance, magneto-thermoelectric effects, polycrystalline Mg₃Bi₂

Received: January 28, 2022

Revised: March 2, 2022

Published online:

- [1] A. V. Ettingshausen, W. Nernst, *Annu. Phys. Chem.* **1886**, 265, 343.
 [2] K. Behnia, H. Aubin, *Rep. Prog. Phys.* **2016**, 79, 046502.
 [3] B. Skinner, L. Fu, *Sci. Adv.* **2018**, 4, eaat2621.
 [4] B. Yan, C. Felser, *Annu. Rev. Condens. Matter Phys.* **2017**, 8, 337.
 [5] B. Qin, D. Wang, X. Liu, Y. Qin, J. Dong, J. Luo, J. Li, W. Liu, G. Tan, X. Tang, J. Li, J. He, L. Zhao, *Science* **2021**, 373, 556.
 [6] J. He, T. M. Tritt, *Science* **2017**, 357, 1.
 [7] Y. Pei, H. Wang, G. J. Snyder, *Adv. Mater.* **2012**, 24, 6125.
 [8] G. Y. Jiang, J. He, T. J. Zhu, C. G. Fu, X. H. Liu, L. P. Hu, X. B. Zhao, *Adv. Funct. Mater.* **2014**, 24, 3776.
 [9] B. Yu, M. Zebajadi, H. Wang, K. Lukas, H. Z. Wang, D. Z. Wang, C. Opeil, M. Dresselhaus, G. Chen, Z. F. Ren, *Nano Lett.* **2012**, 12, 2077.
 [10] J. P. Heremans, C. M. Thrush, D. T. Morelli, *Phys. Rev. B* **2004**, 70, 115334.
 [11] K. Behnia, M. A. Measson, Y. Kopelevich, *Phys. Rev. Lett.* **2007**, 98, 076603.
 [12] W. M. Yim, A. Amith, *Solid-State Electron.* **1972**, 15, 1141.
 [13] Z. Chen, X. Zhang, J. Ren, Z. Zeng, Y. Chen, J. He, L. Chen, Y. Pei, *Nat. Commun.* **2021**, 12, 3837.
 [14] C. G. Fu, Y. Sun, C. Felser, *APL Mater.* **2020**, 8, 040913.
 [15] J. Hu, S.-Y. Xu, N. Ni, Z. Mao, *Annu. Rev. Mater. Res.* **2019**, 49, 207.
 [16] Y. Xu, Z. X. Gan, S. C. Zhang, *Phys. Rev. Lett.* **2014**, 112, 226801.
 [17] C. Shekhar, A. K. Nayak, Y. Sun, M. Schmidt, M. Nicklas, I. Leermakers, U. Zeitler, Y. Skourski, J. Wosnitza, Z. K. Liu, Y. L. Chen, W. Schnelle, H. Borrmann, Y. Grin, C. Felser, B. H. Yan, *Nat. Phys.* **2015**, 11, 645.
 [18] T. Liang, Q. Gibson, M. N. Ali, M. Liu, R. J. Cava, N. P. Ong, *Nat. Mater.* **2014**, 14, 280.
 [19] A. Narayanan, M. D. Watson, S. F. Blake, N. Bruyant, *Phys. Rev. Lett.* **2015**, 114, 117201.
 [20] A. B. Pippard, *Magnetoresistance in Metals*, Cambridge University Press, New York **1989**.
 [21] S. J. Watzman, T. M. McCormick, C. Shekhar, S.-C. Wu, Y. Sun, A. Prakash, C. Felser, N. Trivedi, J. P. Heremans, *Phys. Rev. B* **2018**, 97, 161404.
 [22] C. Fu, S. N. Guin, S. J. Watzman, G. Li, E. Liu, N. Kumar, V. Süß, W. Schnelle, G. Auffermann, C. Shekhar, Y. Sun, J. Gooth, C. Felser, *Energy Environ. Sci.* **2018**, 11, 2813.
 [23] H. Wang, X. Luo, W. Chen, N. Wang, B. Lei, F. Meng, C. Shang, L. Ma, T. Wu, X. Dai, Z. Wang, X. Chen, *Sci. Bull.* **2018**, 63, 411.
 [24] T. Liang, Q. Gibson, J. Xiong, M. Hirschberger, S. P. Koduvayur, R. J. Cava, N. P. Ong, *Nat. Commun.* **2013**, 4, 2696.
 [25] C. G. Fu, S. N. Guin, T. Scaffidi, Y. Sun, R. Saha, S. J. Watzman, A. K. Srivastava, G. W. Li, W. Schnelle, S. S. P. Parkin, C. Felser, J. Gooth, *Research* **2020**, 2020, 4643507.
 [26] X. T. Xu, Y. Y. Liu, G. Seyfarth, A. Pourret, W. L. Ma, H. B. Zhou, G. Q. Wang, Z. Qu, S. Jia, *Phys. Rev. B* **2021**, 104, 115164.
 [27] H. Zhang, C. Q. Xu, X. Ke, *Phys. Rev. B* **2021**, 103, L201101.
 [28] X. T. Xu, X. R. Wang, T. A. Cochran, D. S. Sanchez, G. Q. Chang, I. Belopolski, G. Q. Wang, Y. Y. Liu, H. J. Tien, X. Gui, W. W. Xie, M. Z. Hasan, T. R. Chang, S. Jia, *Phys. Rev. B* **2019**, 100, 045104.
 [29] J. L. Wang, H. Y. Yang, L. C. Ding, W. You, C. Y. Xi, J. Cheng, Z. X. Shi, C. Cao, Y. K. Luo, Z. W. Zhu, J. H. Dai, M. L. Tian, Y. K. Li, *npj Quantum Mater.* **2019**, 4, 58.
 [30] D. Destraz, L. Das, S. S. Tsirkin, Y. Xu, T. Neupert, J. Chang, A. Schilling, A. G. Grushin, J. Kohlbrecher, L. Keller, P. Pupal, E. Pomjakushina, J. S. White, *npj Quantum Mater.* **2020**, 5, 5.
 [31] J. Mao, H. Zhu, Z. Ding, Z. Liu, G. Gamage, G. Chen, Z. Ren, *Science* **2019**, 365, 495.
 [32] X. Zhang, L. Jin, X. Dai, G. Liu, *J. Phys. Chem. Lett.* **2017**, 8, 4814.
 [33] J. Xin, G. Li, G. Auffermann, H. Borrmann, W. Schnelle, J. Gooth, X. Zhao, T. Zhu, C. Felser, C. Fu, *Mater. Today Phys.* **2018**, 7, 61.
 [34] T. Zhou, M. Tong, X. Xie, Y. Yu, X. Zhu, Z. Wang, T. Jiang, *J. Phys. Chem. Lett.* **2020**, 11, 6475.
 [35] Z. Han, Z. Gui, Y. Zhu, P. Qin, B. Zhang, W. Zhang, L. Huang, W. Liu, *Research* **2020**, 2020, 1672051.
 [36] S. Ohno, K. Imasato, S. Anand, H. Tamaki, S. D. Kang, P. Gorai, H. K. Sato, E. S. Toberer, T. Kanno, G. J. Snyder, *Joule* **2018**, 2, 141.
 [37] X. Y. Chong, P. W. Guan, Y. Wang, S. L. Shang, J. P. S. Palma, F. Drymiotis, V. A. Ravi, K. E. Star, J. P. Fleurial, Z. K. Liu, *ACS Appl. Energy Mater.* **2018**, 1, 6600.
 [38] Y. Wang, L. Wang, X. Liu, H. Wu, P. Wang, D. Yan, B. Cheng, Y. Shi, K. Watanabe, T. Taniguchi, S. Liang, F. Miao, *Nano Lett.* **2019**, 19, 3969.
 [39] V. Jovovic, J. Heremans, *Phys. Rev. B* **2008**, 77, 245204.
 [40] A. Pourret, H. Aubin, J. Lesueur, C. Marrache-Kikuchi, L. Berge, L. Dumoulin, K. Behnia, *Phys. Rev. B* **2007**, 76, 214504.
 [41] M. Akhanda, S. Rezaei, *Phys. Rev. Mater.* **2021**, 5, 015403.
 [42] H. Wang, X. Luo, K. Peng, Z. Sun, M. Shi, D. Ma, N. Wang, T. Wu, J. Ying, Z. Wang, X. Chen, *Adv. Funct. Mater.* **2019**, 29, 1902437.

- [43] M. Hashizume, T. Yokouchi, K. Nakagawa, Y. Shiomi, *Phys. Rev. B* **2021**, *104*, 115109.
- [44] Y. Z. Lei, W. Liu, X. Y. Zhou, J. F. Luo, C. Zhang, X. L. Su, G. J. Tan, Y. G. Yan, X. F. Tang, *J. Solid State Chem.* **2020**, *288*, 121453.
- [45] M. Murata, K. Nagase, K. Aoyama, A. Yamamoto, *Appl. Phys. Lett.* **2020**, *117*, 103903.
- [46] M. R. Scudder, B. He, Y. X. Wang, A. Rai, D. G. Cahill, W. Windl, J. P. Heremans, J. E. Goldberger, *Energy Environ. Sci.* **2021**, *14*, 4009.
- [47] M. N. Ali, J. Xiong, S. Flynn, J. Tao, Q. D. Gibson, L. M. Schoop, T. Liang, N. Haldolaarachchige, M. Hirschberger, N. P. Ong, R. J. Cava, *Nature* **2014**, *514*, 205.
- [48] I. D. Bernardo, J. Hellerstedt, C. Liu, G. Akhgar, W. K. Wu, S. Y. A. Yang, D. Culcer, S. K. Mo, S. Adam, M. T. Edmonds, M. S. Fuhrer, *Adv. Mater.* **2021**, *33*, 2005897.
- [49] T. Zhou, X. Zhu, M. Tong, Y. Zhang, X. Luo, X. Xie, W. Feng, Q. Chen, S. Tan, Z. Wang, T. Jiang, Y. Tang, X. Lai, X. Yang, *Chin. Phys. Lett.* **2019**, *36*, 117303.
- [50] N. W. Ashcroft, N. D. Mermin, *Solid State Physics*, Harcourt College, Harcourt, Orlando **1976**.
- [51] J. M. Ziman, *Electrons and Phonons: The Theory of Transport Phenomena in Solids*, Oxford University, Clarendon, Oxford **2001**.
- [52] S. N. Zhang, Q. S. Wu, Y. Liu, O. V. Yazyev, *Phys. Rev. B* **2019**, *99*, 035142.
- [53] Y. Liu, H. J. Zhang, Y. G. Yao, *Phys. Rev. B* **2009**, *79*, 245123.
- [54] L. L. Xi, S. S. Pan, X. Li, Y. L. Xu, J. Y. Ni, X. Sun, J. Yang, J. Luo, J. Y. Xi, W. H. Zhu, X. R. Li, D. Jiang, R. Dronskowski, X. Shi, G. J. Snyder, W. Q. Zhang, *J. Am. Chem. Soc.* **2018**, *140*, 10785.
- [55] G. Kresse, J. Furthmüller, *Comput. Mater. Sci.* **1996**, *6*, 15.
- [56] G. Kresse, J. Furthmüller, *Phys. Rev. B* **1996**, *54*, 11169.
- [57] J. P. Perdew, K. Burke, M. Ernzerhot, *Phys. Rev. Lett.* **1996**, *77*, 3865.
- [58] P. E. Blöchl, *Phys. Rev. B* **1994**, *50*, 17953.
- [59] G. Kresse, D. Joubert, *Phys. Rev. B* **1999**, *59*, 1758.
- [60] A. A. Mostoffi, J. R. Yates, G. Pizzi, Y.-S. Lee, I. Souza, D. Vanderbilt, N. Marzari, *Comput. Phys. Commun.* **2014**, *185*, 2309.
- [61] N. Marzari, D. Vanderbilt, *Phys. Rev. B* **1997**, *56*, 12847.
- [62] I. Souza, N. Marzari, D. Vanderbilt, *Phys. Rev. B* **2001**, *65*, 035109.
- [63] N. Marzari, A. A. Mostoffi, J. R. Yates, I. Souza, D. Vanderbilt, *Rev. Mod. Phys.* **2012**, *84*, 1419.